A baseline study of mineralogical and morphological properties of different size fractions of illite du Puy

Ali Asaad, Fabien Hubert, Baptiste Dazas, Angelina Razafitianamaharavo, Julien Brunet, Martin Glaus, Sébastien Savoye, Eric Ferrage, Emmanuel Tertre

A baseline study of mineralogical and morphological properties of different size fractions of illite du Puy

Ali Asaad[1*], Fabien Hubert[1], Baptiste Dazas[1], Angelina Razafitianamaharavo[2], Julien Brunet[1], Martin A. Glaus[3], Sébastien Savoye[4], Eric Ferrage[1], Emmanuel Tertre[1*]

[1] IC2MP, Equipe HydrASA, UMR 7285 CNRS/Université de Poitiers, 86073 Poitiers, France.

[2] LIEC, UMR 7360 CNRS/Université de Lorraine, BP 40, 54501 Vandoeuvre-lés-Nancy, France

[3] Laboratory for Waste Management, Paul Scherrer Institut (PSI), CH-5232 Villigen PSI, Switzerland.

[4] Université Paris-Saclay, CEA, DES-ISAS-Service d'Etude du Comportement des Radionucléides, F-91191 Gif-sur-Yvette, France.

[*] E-mail addresses of the corresponding authors:

Ali Asaad: ali.asaad@univ-poitiers.fr ; Emmanuel Tertre: emmanuel.tertre@univ-poitiers.fr

Table of Content

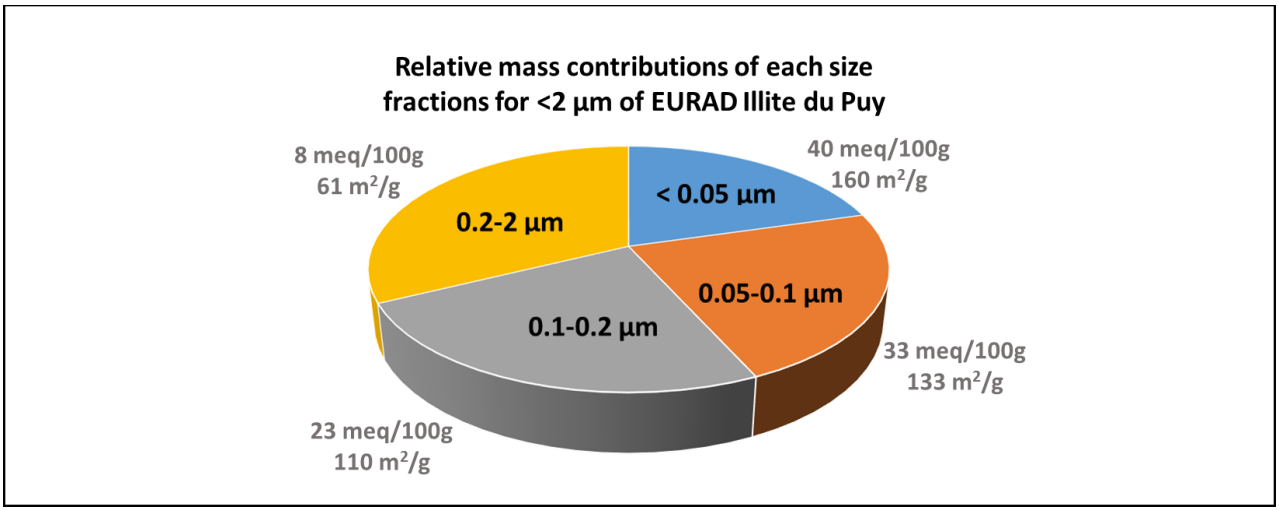

Highlights

- Providing a baseline study of the illite du Puy used in an ongoing European project
- Geological setting is responsible for the mineralogical variability found in the literature
- Particles in the subfractions display similar crystal chemistry and aspect ratios
- The grain density of the illite du Puy particles was revisited and refined

Abstract

The objective of this study is to revisit the mineralogical and physico-chemical properties of illite du Puy material (Puy-en-Velay, France), which is envisaged as a model clay system in the European Joint Programme on Radioactive Waste Management (EURAD) project. This illite material is compared to the raw illite material commonly extracted from the Velay ore site. Both materials were collected and separated into different subfractions (i.e., <0.05, 0.05-0.1, 0.1-0.2, and 0.2-2 µm) to examine the mineralogical heterogeneity. The X-ray diffraction bulk analyses indicated that the observed variability in the literature, in terms of the nature of accessory minerals and the presence of kaolinite, was directly related to the locations of geological sampling. Moreover, the respective mass contributions of the different subfractions were similar for the two materials.

Further analyses were performed on the subfractions of the illite used for the EURAD project by utilizing a suite of different techniques. The clay mineralogy was refined as an illite–smectite mixed-layer mineral with a small amount (<5%) of smectite layers. No significant changes in chemical properties or particle lamellarity were observed between the different subfractions. However, the different subfractions displayed a wide range of specific surface areas (i.e., N_2 BET surface) and cation exchange capacity values, the latter of which increased by factors of ~3 and ~5 from the 0.2-2 µm to the <0.05 µm size fractions, respectively. The EURAD illite and associated subfractions can be considered appropriate material models to be used for the refinement of our understanding of the adsorption and diffusion processes of solutes in porous media made from charged clay particles.

Keywords: illite du Puy, size fractions, mineralogical and morphological properties.

1. Introduction

For the past two decades, purified and conditioned illite du Puy (IDP) has been considered an analogous clay model of more complex clayey rocks (i.e., argillite) envisaged as potential host rocks for the geological disposal of nuclear wastes. Numerous studies have focused on sorption/diffusion of ions and water in this material (Poinssot et al., 1999; Rajec et al., 1999; González Sánchez et al., 2008; Bradbury and Baeyens, 2009; Diaz, 2009; Glaus et al., 2010; Altmann et al., 2015; Rajyaguru, 2018). In these works, the physio-chemical properties of IDP, i.e., mineralogical composition, cation exchange capacity (CEC), specific surface area, and geometrical properties of IDP particles (the relative amount of lateral and basal surfaces; Bardot et al., 1998; Rajec et al., 1999; Hassan et al., 2005) represented key input parameters for the interpretation of anionic exclusion and sorption reactions for solutes (e.g., Bradbury and Baeyens, 2005, 2009; Rabung et al., 2005; González Sánchez et al., 2008; Glaus et al., 2010, 2015; Altmann et al., 2015; Chagneau et al., 2015). Despite the large number of studies devoted to IDP, significant differences in the composition and thus reactive properties of this material can be found in the literature. For example, Poinssot et al. (1999) reported the presence of kaolinite at ~5% and 7% in raw and purified Na^+-saturated IDP, respectively, as observed by X-ray diffraction (XRD) and Fourier transform infrared spectrometry (FTIR). In contrast, Bradbury and Baeyens (2009) and Altmann et al. (2015) reported a composition of Na^+-saturated IDP of 88 wt.% illite and 12 wt.% sanidine (K-feldspar), which was also deduced from XRD measurements. Even though some of the reported variations in CEC and specific surface area can be induced by the differences in the processes used to purify the raw material (e.g., size separation and removal of accessory minerals), another reason for these differences may be the variation in the mineralogical properties of the raw material in relation to the geological setting and sampling strategy.

IDP originates from the Velay basin, which consists in Oligocene lacustrine sediments of approximately thirty kilometers in length located at le Puy-en-Velay (Haute-Loire) in the Massif Central region in France. The first mineralogical study of this basin was carried out by Gabis (1963), who divided the central area of this geological formation into three series: upper, lower, and medium series (30-80 m thick). According to this author, deposits from these series are predominantly composed of ferruginous illite that results from the illitization of detrital montmorillonite in alkaline lakes. In addition to illite, associated clay minerals may include (i) kaolinite in a proportion up to 20% in the bottom of the series, this percentage decreasing moving upward until kaolinite diminishes in the upper portion (Gabis, 1963); (ii) illite-smectite mixed-layer minerals with low smectite contents (~20 to 30%; Altmann et al., 2015); and (iii) smectite, which is mainly present in the upper portion. Other non-clay accessory minerals include potassic feldspars (mainly sanidine (Bradbury and Baeyens, 2009)), carbonates, and quartz, in varying proportions from 0 to 40%. In addition to their presence at the clayey levels, carbonates also exist in the banks of gray marl and calcite streaks, intercalating with the clay-rich levels. Some of these latter in the medium series exhibit remarkable mineralogy that is solely composed of illite. Overall, and although illite is the dominant mineral through the stratigraphic profile, the other associated minerals in IDP material may vary significantly with the location and sampling strategy applied in the field.

In the context of nuclear waste disposal facilities, and before the analysis of sorption and diffusion properties of water and ionic tracers in IDP material, a particular attention must be paid to the sampling and to the associated characterization of these material. In fact, these properties may vary due to the variability in mineralogical composition of IDP raw material when sourced from different geological settings. In the framework of the European Joint Program on Radioactive Waste Management (EURAD, 2019-2024), a large set of studies

involving adsorption and diffusion measurement of a large set of tracers using the same IDP raw material stresses the need for a baseline analysis of IDP mineralogical and physico-chemical properties. Hence, this study aims to (i) elucidate the differences in mineralogy between the IDP material used in EURAD and typical sampling in the Velay ore used in previous works and then (ii) to determine the mineralogy, crystal chemistry, and geometric characteristics of the IDP particles used in the current EURAD project as an analogous illite model. An initial quantitative mineralogical analysis of both IDP raw materials will be performed for these purposes. Afterward, both raw materials will be purified and size-fractionated (i.e., <0.05, 0.05-0.1, 0.1-0.2, and 0.2-2 µm) to highlight the mineralogical heterogeneity between the different size fractions. After a mineralogical comparison between the two IDP samples, a detailed characterization that focuses on the different subfractions of the IDP sample used in the EURAD project will be provided, including (i) clay structure identification and smectite quantification by profile modeling of XRD 00ℓ reflections, (ii) structural formula and grain density calculations based on microchemical analysis by scanning electron microscopy (SEM) equipped with energy dispersive X-ray spectroscopy (EDX), (iii) specific surface area measurements and associated geometrical features of particles from low-pressure N_2/Ar adsorption at 77 K and (iv) CEC measurements from K^+-saturated samples. The results from this work will be compared to the literature data to establish a baseline source of physico-chemical data of interest for the use of IDP as a model material to expand our understanding of the transport properties of solutes in the context of nuclear waste disposal facilities.

2. Materials and Methods

2.1. Illite du Puy materials

Three raw IDP samples were considered for this study, all originating from Oligocene lacustrine sediments in le Puy-en-Velay (Haute-Loire, France). The Argile du Velay company (www.argileduvelay.com) provided the first IDP sample collected from the clay ore during industrial sampling. The second IDP sample was provided by the Paul Scherrer Institute (PSI, Villigen, Switzerland) from its sampling campaign and corresponded to the reference illite used in their own work (González Sánchez et al., 2008; Bradbury and Baeyens, 2009), in the CatClay European project (Glaus et al., 2010, 2015; Altmann et al., 2015 among others) and in the ongoing European Join Project EURAD. The third IDP material was provided by the Commissariat à l'énergie atomique (CEA, Université Paris-Saclay, France) from their sampling campaign, which was used in previous works (Poinssot et al., 1999). However, different previous mineralogical analyses on this last sample revealed a similar composition to the Velay IDP (data not shown). Consequently, only a comparison between data obtained with the Velay and EURAD IDP will be presented here.

For sample homogenization of raw materials before bulk mineral quantification using X-ray diffraction (XRD) on randomly oriented powder, the Velay and EURAD IDP samples (referred to as V-IDP and E-IDP materials, respectively) were gently crushed in an agate mortar and dry sieved at 50 µm. To perform other analyses, raw IDP samples were purified and size-fractionated. The purification procedure consisted of removing carbonate and sparingly soluble minerals by mixing clay dispersion in hydrochloric acid (pH=1, room temperature). Carbonate dissolution was considered complete when the pH of the clay/acid suspension reached 5.5. A confirmation of the complete removal of carbonates was obtained by recording the XRD patterns (not shown) of the decarbonated material. The < 50 µm particle size fraction of the

153 decarbonated IDP was obtained by wet sieving after several cycles of centrifugation with
154 distilled water to remove the remaining acidic solution. Then, the Na^+ saturation of IDP samples
155 was achieved by performing three saturation cycles with a 1 M NaCl solution followed by
156 removing excess salt by dialysis using a 6-8 KD membrane until the test with silver nitrate was
157 negative. Different size fractions were obtained from the dispersion of the Na^+-saturated IDP
158 samples by adapting the protocol of sequential fractionation developed by Reinholdt et al.
159 (2013). The <2 µm fraction was first separated using a Thermo Scientific legend XFR
160 centrifuge from Fisher Scientific®. Then, 5 g of <2 µm IDP were divided between 6
161 centrifugation tubes (38.5 mL polypropylene tubes), dispersed in Milli-Q® pure water by
162 sonication, and centrifuged using an Avanti J 301 centrifuge (swinging bucket rotor JS-24.38)
163 from Beckman Coulter®. The sequential fractionation process started with extraction of the
164 finest fraction (i.e., <0.05 µm), and five centrifugation cycles were performed until the
165 supernatant became clear. Then, extractions of the coarser size fractions (0.05-0.1 and 0.1-0.2
166 µm) were performed using the same steps until the IDP material remaining in the tubes
167 corresponded to the 0.2-2 µm fraction. Three aliquots of dispersion (1 mL) from each fraction
168 were dried at ambient humidity and weighed to calculate the mass proportions. The
169 centrifugation parameters and the yield of each size fraction are reported in Table 1.

170 After size separation, the obtained dispersion of each fraction was divided into three
171 portions. Two of them were saturated with Ca^{2+} and K^+ for XRD and CEC measurements,
172 respectively, by following the same procedure described above for saturation with Na^+. The
173 Ca^{2+}- and K^+-saturated IDP samples were stored in suspension at 4 °C. The last portion, which
174 corresponded to the remaining Na^+-saturated dispersion, was lyophilized for gas adsorption
175 measurements as described in Section 2.5.

176

177 **Table 1**. Centrifuging parameters for size fractioning of the Velay and EURAD illite du Puy
178 samples (V-IDP and E-IDP, respectively) and the relative mass contributions of each size
179 fraction.

Fraction (µm)	Time (min)	Speed (rpm)	Acceleration (g)	% Mass contribution[a]	
				V-IDP	E-IDP
<0.05	20	20000	72128	19.5	18.2
0.05-0.1	15	12500	28175	23.8	20.1
0.1-0.2	14	6500	7619	22.1	21.7
0.2-2	-	-	-	22.0	28.6
<2	3	1000	-	-	-
2-50	-	-	-	6.0	6.5
			Total Yield %	93.4	95.1

180 [a] Uncertainties in relative mass contributions are estimated at ~10% (based on replicate measurements).

181

182 ### *2.2. Bulk mineral quantification using XRD refinement on randomly oriented powders*

183 The XRD randomly oriented mounts for V-IDP and E-IDP bulk materials were prepared
184 by filling the sample holder using the side-loading technique as in Kleeberg et al. (2008).
185 Acquisition of XRD patterns of these samples was performed with a Bruker D8 Advance
186 operating in Bragg–Brentano geometry using a copper source with CuKα_{1+2} wavelength and
187 with a LYNXEYE detector for a step size of 0.02°2θ over the 2−65°2θ CuKα angular range. A
188 40 kV voltage and 40 mA intensity were used for the analytical conditions. Crystalline phase
189 quantification was carried out using the open-source Rietveld refinement program BGMN
190 interfaced with Profex (Doebelin and Kleeberg, 2015). In both refinements, illite was modeled
191 using a combination of both disordered and ordered 1M polytypes with a chemical composition
192 that matched the structural formula reported in the present study. The presence of K-feldspars
193 was modeled by considering a mixture of sanidine and microcline (Gabis, 1963; Bradbury and
194 Baeyens, 2009). Other minerals included Na-rich plagioclase (oligoclase; (Gabis, 1963)),

calcite, with trace amounts of quartz, anatase and apatite. The R_{wp} goodness of fit parameter was used for the refinement (Howard and Preston, 1989).

2.3. Quantification of clay mineralogy using profile modeling of XRD 00ℓ reflections

The characterization of the clay phases in the different E-IDP size fractions was obtained by XRD analysis of the oriented clay mounts. An aliquot of the Ca^{2+}-saturated clay dispersion was dropped onto a glass slide and dried at room temperature. The XRD patterns were recorded using a Panalytical X'Pert Pro MPD diffractometer equipped with an X'Celerator detector operating with an angular aperture of 1.021°. The scanning parameters included a step size of 0.033°2θ and 6 s for the counting time per step throughout the 2-50°2θ CuKα_{1+2} angular range. The divergence slit, the anti-scatter slit, and the two Soller slits were 0.125°, 0.25°, 2.3°, and 2.3°, respectively. For all samples, XRD patterns were recorded in air-dried (AD) conditions and after ethylene glycol (EG) saturation of the clay mounts in an EG atmosphere at 40 °C for 24 h.

The algorithms developed initially by Sakharov and coworkers were used to model the 00ℓ reflections for the 2–50°2θ CuKα range using a trial-and-error approach (Sakharov et al., 1982a, 1982b, 1983). Instrumental and experimental factors, such as horizontal and vertical beam divergences, goniometer radius, and length and thickness of the oriented slides, were measured and introduced without further adjustment. The mass absorption coefficient was set to 45 cm^2/g (Moore and Reynolds, 1997). For each XRD pattern, a single illite–smectite interstratified structure was used. Structural parameters, such as the proportion of illite layers, layer-to-layer (LLT) distance of illite layers, and coherent scattering domain size (CSDS) along the c* axis (which was characterized by a lognormal distribution around a variable mean value (N) and a maximum CSDS value set to 80 layers (Drits, 1997)), were adjusted to fit the

218 experimental XRD patterns. The z-coordinates for all atoms within the 2:1 layer framework
219 were set as suggested by Moore and Reynolds (Moore and Reynolds, 1997). The chemical
220 composition was introduced according to the IDP structural formula reported in this work. The
221 interlayer configuration of smectite was systematically constituted by 2 layers of water or EG
222 molecules in AD (LLT=15 Å) and EG conditions (LLT=16.9 Å), respectively.

223

224 **2.4. *Microchemical analysis by electron microscopy***

225 Microchemical analysis was performed on compressed pellets of clay powders from the
226 E-IDP subfractions using a JEOL JSM IT500 scanning electron microscope (SEM) equipped
227 with a Bruker Lynxeye Energy Dispersive X-ray spectrometer (EDX) with an XFlash 4030
228 silicon drift detector. The acquisition parameters for quantitative EDX analysis were as follows:
229 acceleration voltage 15 kV, current beam 1 nA, counting time 50 s, working distance 11 mm,
230 and analytical area of ~ 2 µm. The quality of the EDX quantitative analysis was confirmed by
231 a series of standards consisting of albite (Na, Al, Si), almandine (Mg, Fe), diopside (Ca),
232 orthoclase (K), and spessartite (Mn). Matrix corrections were performed using the integrated
233 program PhiRhoz correction. The reproducibility of the standard analyses was 1.5% for all
234 chemical elements, except Na, for which the reproducibility was 3%.

235

236 ***2.5. Low-pressure nitrogen and argon adsorption at 77 K***

237 Low-pressure nitrogen (N_2) and argon (Ar) adsorption measurements of the E-IDP
238 fractions were performed at LIEC (Laboratoire Interdisciplinaire des Environnements
239 Continentaux) Nancy-France. The experimental procedure consists on the recording of high-
240 resolution adsorption isotherms on a lab-built automatic quasi-equilibrium volumetric setup,

described elsewhere (Michot et al., 1990; Villiéras et al., 1997; Bardot, 1998). The quasi-equilibrium technique is based on the adsorbate introduction with a slow, constant, and continuous flow rate through a micro leak. High-resolution adsorption isotherms were recorded at least up to the BET domain, corresponding to the formation of the first adsorbed layer.

Before adsorption measurements, the E-IDP size fractions were flash-frozen by immersion in slush nitrogen (SN_2) for 2-5 min and dried by lyophilization at – 40 °C. All samples were first outgassed at a 10^{-5} Pa residual pressure for at least 12 h at 110 °C to remove surface impurities. The use of two probe molecules, argon and nitrogen, and the capacity of the experimental setup to record approximately 3000 adsorption points (i) allows for cross-validation of the overall surface area of the particles while (ii) giving access to morphological properties of the clay particles, such as the area of basal/lateral surfaces and the aspect ratio (the ratio between the particle thickness and diameter).

Due to a large number of experimental data points, the experimental derivative adsorption isotherms can be calculated as a function of the logarithm of relative pressure, $\ln(P/P_0)$, which corresponds to the adsorption energy expressed in kT or RT units. These isotherms were analyzed by the derivative isotherm summary (DIS) procedures introduced by Villieras et al. (1992) and later improved by others (Villieras et al., 1997; Bardot et al., 1998). This procedure allows for the study of energetic surface heterogeneity in highly heterogeneous materials such as clay particles. DIS is performed by fitting the experimental derivative isotherm to local theoretical isotherms that correspond to different adsorption energy domains (basal and lateral faces). Each local derivative isotherm is defined by three parameters (Bardot, 1998): the interaction energy between the solid and the adsorbed molecule, which is deduced from the peak position of ($\ln P/P_0$), the lateral interaction between two adjacent gas molecules (ω), and

264 the monolayer capacity (V_m) of the domain, which can be used to calculate the surface area by
265 taking into account cross-sectional areas of 13.8 $Å^2$ and 16.2 $Å^2$ for argon and nitrogen
266 molecules, respectively.

267 Mean particle thickness (*h*) and basal diameter (*l*) were calculated by considering IDP
268 particles as regular hexagonal plates using the equations reported in Hassan et al. (2005):

269 $$h = \frac{2}{\rho \times BSA} \quad (1)$$

270 $$l = \frac{8}{\sqrt{3} \times \rho \times LSA} \quad (2)$$

271 where BSA and LSA are the basal and lateral surface areas from low-pressure Ar
272 measurements, respectively, and ρ is the grain density of the Na^+-saturated E-IDP particles,
273 which is calculated for the different subfractions by using structural formulas and crystal
274 structure parameters derived in this study from the XRD structural refinements.

275 ### *2.6. Cation exchange capacity (CEC) measurements*

276 The first attempts to measure the CEC values from Na^+-saturated samples and Ca^{2+}-for-
277 Na^+ exchange proved unsuccessful. Indeed, the results showed a decrease in CEC with
278 decreasing size fraction. This behavior was attributed to the difficulty in saturating the edge
279 sites of IDP particles with Na^+ cations at neutral pH because of the higher selectivity of H^+ over
280 Na^+ for this type of sites (Tertre et al., 2011b, 2011a). Thus, to ensure sufficient saturation of
281 edge sites in these conditions, the CEC values were obtained from K^+-saturated samples and
282 Sr^{2+}-for-K^+ exchange (Viennet, 2015). Known masses of the K^+-saturated size fractions
283 (ranging from ~30 mg for the finest size fraction to ~100 mg for the coarsest fraction) were
284 dispersed in 100 mL of 1 M $SrCl_2$ prepared with Milli-Q® pure water (18 MΩ·cm). The

dispersions were mechanically agitated and allowed to react for one week. The clay slurry was then retrieved by centrifugation at 34000 g for 30 min (Centrifuge Avanti J 301, rotor JLA-16.250 from Beckman Coulter®) to ensure that no fine particles were left in the supernatant. The K^+ concentrations of the collected supernatants were measured by atomic absorption spectroscopy (AAS, Varian AA240FS). For analysis, the supernatants were diluted with 2% HNO_3, and were prepared in 2 g/L $CsNO_3$ solution to account for possible interference during acquisitions. The measured K^+ concentrations ranged between 1-3 mg/L, which felt within the linear absorption range of K^+ for this device (between 0 and 5 mg/L). The excess $SrCl_2$ salt present in each clay slurry was removed by dialysis in Milli-Q® pure water using a 6-8 KD membrane until the test with silver nitrate was negative. Then, the rinsed clay slurry was dried at 60 °C to determine the dry clay mass, which was found to be similar to the initial mass of the solid from the original dispersion with an uncertainty of ~6 wt%. Measuring the solid mass before and after CEC measurements allowed us to discard any influence of mineral dissolution during the dialysis procedure. Such uncertainty, combined with the one from aqueous concentrations measured by AAS (i.e., 5%), led to a global uncertainty value of approximately 10% for each calculated CEC value.

3. Results and discussion

3.1. Mineralogy comparison between V-IDP and E-IDP raw materials

Fig. 1a shows a comparison between the XRD patterns from randomly oriented powders of the raw V-IDP and E-IDP materials. Both XRD patterns exhibit the typical reflections of illite and K-feldspars, while the V-IDP pattern presents additional reflections for kaolinite and calcite. Full pattern Rietveld refinement (Fig. 1b) shows that the raw E-IDP sample is mainly

308 composed of 1M illite polytype (~83%), with ~15% feldspars (plagioclase, sanidine, and
309 microcline). This sample also contains small quantities of quartz with the addition of <1% each
310 of anatase, halite, and apatite. The raw V-IDP samples are also dominated by 1M illite (~81%),
311 with a small quantity of quartz, anatase, and apatite. The main differences found in the raw V-
312 IDP sample are a lower amount of feldspars (7.5%) and significant contributions of calcite and
313 kaolinite of ~5 and 4%, respectively. Phase quantification, particularly the absence of calcite
314 and kaolinite in the E-IDP sample, allows us to consider this sample similar to the material used
315 by previous authors (Tessier, 1984; Bardot, 1998; Bardot et al., 1998; Rajec et al., 1999; Hassan
316 et al., 2005; Bradbury and Baeyens, 2009; Altmann et al., 2015). By comparison, the
317 mineralogical composition of the V-IDP sample with large amounts of kaolinite corresponds to
318 that of the sample used by Poinssot et al. (1999), Diaz (2009), and Rajyaguru (2018). By
319 comparing the experimental XRD patterns reported in Gabis (1963) to those obtained in this
320 work, it was found that both IDP samples come from the middle series of the central zone of
321 the Velay sedimentary basin (Fig. 2). More precisely, the E-IDP sample likely belongs to the
322 "green clay" level, which alternates with the marl banks in the middle of this series. In addition,
323 according to Gabis (1963), this level does not contain calcite minerals, unlike the beds just
324 above or below it. The presence of kaolinite in the raw V-IDP sample suggests that it comes
325 from the "versicolored clayey banks" below the "green clay" level, where illite and kaolinite
326 form a mixture that contains 5-10% calcite (Fig. 2).

327 With more than 80% of their mass being illite mineral, both of the raw IDP samples are
328 appropriate candidates for reference illitic material. Naturally, the removal of the other non-
329 illitic minerals is necessary. A simple and widely used method for purifying clay materials is
330 size separation after dispersion and removal of soluble minerals (e.g., calcite). In this work, the
331 results from sequential fractionation indicate (i) that both IDP samples are widely dominated

by <2 µm particles (values normalized to the total yield at 94 and 93% for V-IDP and E-IDP samples, respectively; Table 1), and (ii) that each of the <2 µm subfractions has a significant mass contribution of more than 18%. However, the 0.2-2 µm size fraction has ~5% higher mass contribution in the E-IDP sample (Table 1). As commonly observed in natural clay samples (Hubert et al., 2012; Viennet et al., 2015), the XRD patterns of the fine <0.2 µm subfractions (Fig. 3) indicate that both IDP samples are almost entirely constituted from clay phases, while the accessory silicates remain concentrated in the 0.2-2 µm fraction. However, this method did not allow to separate kaolinite from the different subfractions of the V-IDP sample, given that kaolinite persists even in the finest fraction that was investigated (i.e., <0.05 µm). It is worth noting that kaolinite traces remained even in <0.02 µm fraction for the V-IDP sample (results not shown). In contrast, the <0.2 µm subfractions of the E-IDP sample exhibit only 00ℓ reflections of illite, and a quasi-monomineralic sample of illite is thus obtained. Therefore, the minimal shifts of the 00ℓ reflections of illite after ethylene glycol solvation indicate that the illite phase of both IDP samples is most likely an illite–smectite mixed-layer mineral (MLM) mainly composed of illite layers with a marginal proportion of smectite layers (Fig. 3). This illite–smectite mixed-layer mineral is present in all size fractions. The broadening of its 00ℓ reflections with decreasing particle size is most likely because of the decrease in the coherent scattering domain size, as previously observed for size fractionation of vermiculite (Reinholdt et al., 2013).

The mineralogical results show that a large amount of quasi-monomineral illite material can be obtained easily from raw E-IDP by size fractionation at <0.2 µm (representing ~60% of raw E-IDP mass). Note that removing other clay minerals, such as kaolinite, from the 0.2 µm and other subfractions is not achievable by using the approach used here based on size fractionation.

In line with the main objectives of this work, the following sections provide further analysis of the subfractions of the E-IDP used in the EURAD project. These analyses include information on the crystal structure, grain density, particle morphology, CEC, and crystal chemistry of these size fractions.

3.2. Chemical properties and geometrical characterization of subfractions from the E-IDP sample

3.2.1. Crystal structure of illite–smectite MLM in E-IDP size fractions

The crystal structure of the illite phase in the different size fractions of E-IDP material was determined by profile modeling of the 00ℓ reflections on XRD patterns recorded after AD and EG treatments (Fig. 4). A single R0 illite–smectite MLM was sufficient to reproduce the experimental XRD profiles of the 00ℓ reflections in the different subfractions and for both treatments. As reported in Table 2, this illite–smectite MLM contains an overwhelming proportion of illite layers with a very low proportion of smectite layers, which is lower than 5% irrespective of the size fraction. Except for the marginal increase of 1% of smectite layers, the main evolution of crystal structure with the decrease of particle size is the aforementioned gradual decrease of the mean CSDS, from 14 layers (in the EG state) for the coarsest 0.2-2 µm fraction to ~7 layers for the <0.05 µm size fraction. Note that the slight increase in the smectite layer content after EG saturation is consistent with the swelling of smectitic layers that were initially collapsed in the AD state (Ferrage et al., 2011).

The different size fractions of the E-IDP sample are thus composed of a single type of clay mineral, i.e., an R0 illite–smectite MLM. Compared to materials mentioned in previous studies that contain a proportion of smectite layers that can reach nearly 20 to 30% (Altmann et al., 2015), the illite–smectite MLM of the E-IDP sample is particularly rich in illite layers

with less than 5% smectite layers. Moreover, the crystal structure of the illite–smectite MLM is notably stable despite the changes in particle size. Indeed, only a decrease in CSDS is correlated with a particle size decrease, as generally previously observed (Hubert et al., 2012; Viennet et al., 2015; Bakker et al., 2019).

Table 2. Structural parameters for the modeling of experimental 00ℓ XRD reflections of Ca^{2+}-saturated fractions of EURAD illite du Puy (E-IDP) in air-dried conditions (AD) and after ethylene glycol saturation (EG).

	AD			EG		
Fraction (µm)	% I/S[a]	N[b]	LLT Illite[c]	% I/S	N	LLT Illite
<0.05	97/3	7	9.97	96/4	7.6	9.97
0.05-0.1	97/3	8.2	9.98	96/4	9	9.98
0.1-0.2	97/3	9.3	9.99	97/3	10	9.99
0.2-2	98/2	12	10	97/3	14	10

[a] relative proportion of illite and smectite layers. [b] Coherent scattering domain size value (in layers). [c] Layer-to-layer distance of illite layers (in Å).

3.2.2. Structural formulas and grain densities of E-IDP size fractions

Energy dispersive spectrometric (EDS) measurements of the compressed pellets of dry powder from the different fractions of the E-IDP sample were obtained by scanning electron microscopy. All size fractions, which were initially Ca^{2+}-saturated for mineralogical characterization, were Na^{+}-saturated, except for the <2 µm fraction. The structural formula for each fraction is reported in Table 3. During SEM observations of the compacted pellets, a dispersion of small grains of titanium oxides between clay particles was detected. Therefore, TiO_2 quantities were removed from the calculation of the structural formula. Moreover, as both the 0.2-2 and the <2 µm fractions contain feldspar impurities, the reported chemical

composition does not correspond to pure illite minerals but corresponds more closely to a mixture of phases for these two size fractions.

Table 3. Structural formulas and grain densities for different size fractions of EURAD illite du Puy (E-IDP).

Size fraction (µm)	Structural Formula [a]	Interlayer charge (per $O_{20}(OH)_4$)	Calculated grain density ($g.cm^{-3}$)
<0.05	$[Al_{2.69}Mg_{0.78}Fe_{0.60}]_{\Sigma 4.08}$ $(Si_{7.24}Al_{0.76})$ $O_{20}(OH)_4$ $(K_{1.19}Na_{0.08}Ca_{0.02})$	1.30	2.79
0.05-0.1	$[Al_{2.51}Mg_{0.80}Fe_{0.79}]_{\Sigma 4.10}$ $(Si_{7.07}Al_{0.93})$ $O_{20}(OH)_4$ $(K_{1.16}Na_{0.08}Ca_{0.09})$	1.42	2.82
0.1-0.2	$[Al_{2.46}Mg_{0.79}Fe_{0.81}]_{\Sigma 4.06}$ $(Si_{6.98}Al_{1.02})$ $O_{20}(OH)_4$ $(K_{1.31}Na_{0.19}Ca_{0.05})$	1.60	2.83
0.2-2 [b]	$[Al_{2.52}Mg_{0.74}Fe_{0.76}]_{\Sigma 4.02}$ $(Si_{6.95}Al_{1.05})$ $O_{20}(OH)_4$ $(K_{1.55}Na_{0.06}Ca_{0.05})$	1.71	2.84
<2 [b]	$[Al_{2.50}Mg_{0.75}Fe_{0.80}]_{\Sigma 4.04}$ $(Si_{7.02}Al_{0.98})$ $O_{20}(OH)_4$ $(K_{1.33}Na_{0.02}Ca_{0.11})$	1.57	2.83

[a] Fe is considered as Fe^{3+}
[b] samples contain minor amounts of K-feldspars

The deduced structural formulas are typical of ferruginous illitic material (Gabis, 1963; Tessier, 1984) with an increased Fe^{3+} occupation in the octahedral sheet that correlates to a decrease in Al^{3+} content. There is a slight increase in Si^{4+} in the tetrahedral sheet upon comparison to what is reported in the literature (Wilson, 2013). In addition, the octahedral occupancy is slightly higher than 4, which can be attributed to the presence of small trioctahedral domains. Finally, for the three <0.2 µm fractions, which are more representative of a pure illitic phase, note that the layer charge decreases with decreasing size fraction (Table 3). Such a decrease of this value for the finest illitic clay fraction was previously reported for

illite material collected from soil environments (Robert et al., 1991). This observation can be tentatively assigned to the formation conditions of the particles and the slight increase in smectite contribution in the finest fractions (Table 2). Another observation is the remaining Ca^{2+} amount, which can be tentatively associated to adsorption sites in the smectite or illite interlayers and on the external surface of particles (Table 3). Overall, the structural formulas obtained for all subfractions are consistent with those reported in the literature and derived from different methods (Gabis, 1963; Tessier, 1984; Bardot, 1998; Poinssot et al., 1999; Altmann et al., 2015). Minor differences can be assigned to the selection of the size fractions and sampling region in the ore site.

Grain densities for the different subfractions were calculated based on the structural formula (Table 3) and cell parameters derived in this study. Densities for both ordered and disordered illite were calculated by taking into account *a* and *b* parameters obtained from the bulk refinement for each of these polytypes (i.e., a = 5.165 Å and b = 8.996 Å for ordered illite and a = 5.2269 Å and b = 9.049 Å for disordered illite), and densities values reported in Table 3 are averaged values based on the contribution of these two polytypes in each subfraction. For these calculations, layer-to-layer distances reported in Table 2 for each subfraction and corresponding to c^* parameters were used. The calculated grain densities show no noticeable variation with particle size (Table 3). A mean grain density value of the <2 µm fraction at 2.83 $g.cm^{-3}$ can be calculated based on the relative proportion of the different subfractions. This value is slightly higher than the grain density of ~2.7-2.79 $g.cm^{-3}$ that was reported in the literature (Tessier, 1984; Bardot, 1998; Poinssot et al., 1999; Altmann et al., 2015) based on generic compositions and structural parameters.

435 3.2.3. *Specific surface area and associated geometrical features of particles in E-IDP size*
436 *fractions*

437 The derivative isotherms of low-pressure argon adsorption at 77 K and the DIS
438 decomposition for the different size fractions of Na^+-saturated E-IDP are shown in Fig. 5. The
439 parameters used for the DIS modeling are reported in Table S1 (see Supplementary Data
440 (S.D.)). The lateral, basal, and total specific surface areas (LSA, BSA, and TSA, respectively)
441 from the DIS decomposition are reported in Table 4. This table also includes the mean values
442 for the height (*h*) and basal length (*l*) of the clay particles, which were calculated according to
443 Eqs. 1 and 2, respectively, based on the grain densities reported in Table 3.

444 The experimental derivative isotherms are similar for all size fractions, and the
445 decomposition procedure leads to the definition of 6 and 5 energy domains for the <0.1 µm and
446 >0.1 µm fractions, respectively (Table S1). These different domains are attributed to either
447 lateral (green dashed line; Fig. 5) or basal (red dashed line; Fig. 5) surfaces (Michot et al., 1990;
448 Villieras et al., 1992, 1997; Bardot et al., 1998; Chemeda et al., 2021). The overall TSA values
449 expectedly increase with decreasing size fraction and are consistent with the N_2 adsorption
450 results (Table 4) upon consideration of the differences between the acquisition methods
451 (continuous vs. point-by-point method for N_2 and Ar, respectively).

452 Mean particle lengths and heights derived from the DIS decomposition are found to
453 decrease with decreasing size fractions. The obtained mean particle dimensions are in fair
454 agreement with those reported by Rajec et al. (1999) and Hassan et al. (2005) for the same
455 material, although no size fractionation was performed in these previous studies. The aspect
456 ratio of ~0.1 obtained for <0.2 µm size fractions in this study is also in good agreement with
457 the results of these previous studies (Rajec et al., 1999; Hassan et al., 2005). Note that the aspect
458 ratio value is slightly higher for the 0.2-2 µm size fraction, which can be associated to the

presence of non-clay accessory minerals (Fig. 1b). Interestingly, the aspect ratio for the <0.2 µm size subfractions is similar to that obtained for Santa Olalla vermiculite by Reinholdt et al. (2013). These authors indeed reported an aspect ratio of 0.08 and a TSA value of ~108 $m^2.g^{-1}$ for the dried Na^+-saturated 0.1-0.2 µm size fraction of vermiculite, which is in good agreement with the results obtained for the same size fraction of E-IDP. This finding is of particular interest in the scope of investigating the influence of interlayer porosity on a given process (e.g., adsorption or diffusion of solute species in porous clay media) for specific particle sizes and morphologies.

Table 4. Physico-chemical characterization of Na^+-saturated size fractions of EURAD illite du Puy (E-IDP) with relative mass contributions to the <2 µm size fraction, cationic exchange capacity values, and geometrical properties. Surface measurements include the total specific surface area determined by both N_2 and Ar adsorption. Particle geometry analysis includes lateral and basal specific surface areas (LSA and BSA, respectively) and the height (*h*) and basal length (*l*) of clay particles obtained by low-pressure Ar adsorption and DIS decomposition.

Sample		This study						Hassan et al. (2005)[e]	Rajec et al. (1999)[f]
		<0.05 µm	0.05-0.1 µm	0.1-0.2 µm	0.2-2 µm	<2 µm	<2 µm[calc.]	IDP	IDP
Relative mass contribution to <2 µm (%)[a]		0.21	0.23	0.24	0.32	-	-	-	-
CEC[b] (meq/100 g at pH = 7)		39.5	32.7	22.8	8.4	21.2	24.0	-	-
N_2 TSA ($m^2.g^{-1}$)[c]		184.6	153	114.1	60.8	123.6	120.8	-	-
Ar specific surface area ($m^2.g^{-1}$)[c]	Total (TSA)	158.2	133.2	109.2	60.7	-	-	171	233
	Lateral (LSA)	30.4	27.3	16.7	15.6	-	-	38	29
	Basal (BSA)	127.8	105.9	92.5	45.1	-	-	133	
Geometrical parameters of particles from DIS decomposition	*h* (nm)[d]	5.5	6.5	7.4	16.4	-	-	5.7	3.6
	l (nm)[d]	53.1	58.3	94.7	109.7	-	-	46.4	52.0
	aspect ratio (*h*/*l*)	0.10	0.11	0.08	0.15	-	-	0.12	0.07

[a] uncertainties calculated at ~10% (based on replicate measurements), [b] uncertainties calculated at ~10% (taking into account uncertainties on sample dry mass and measured aqueous concentration), [c] uncertainty on external specific area values of ± 1 $m^2.g^{-1}$, [d] calculated using Eqs. 1 and 2, [e & f] calculated from fixed cations per $O_{10}(OH)_2$.

3.2.4. *The cation exchange capacity of E-IDP size fractions*

The measured CEC values of the different size fractions of E-IDP, reported in Table 4, show an expected increasing trend with decreasing particle size. In that regard, the CEC, mainly originating from the sorption sites on the particle external surfaces, agrees with the evolution

494 of the N_2 or Ar TSA values. To further validate our results, the obtained CEC values for the
495 <2 µm size fraction can be successfully compared to the calculated values (<2 $µm^{calc.}$) based on
496 the relative proportion and associated CEC values of each subfraction (Table 4). This very good
497 agreement between the experimental and calculated CEC values is also obtained for N_2 TSA
498 values between <2 µm and <2 $µm^{calc.}$ fractions, further confirming the consistency of the results
499 derived for the different subfractions (Table 4).

500 The results obtained in this study for E-IDP can be compared to those obtained by
501 Altmann et al. (2015) using similar materials. These authors reported a CEC value of 19
502 meq/100 g and an N_2 TSA value of 110 $m^2.g^{-1}$ for the Na^+-saturated sample. Both values are in
503 good agreement with our results, although Altmann et al. (2015) reported a different mineralogy
504 of the clay phase with a large amount of smectitic layers (20-30% vs. <5% in the present study).
505 In contrast, the lower CEC and N_2 TSA values reported by Poinssot et al. (1999) for V-IDP
506 (13.2 meq/100 g and a N_2 TSA value of 97 $m^2.g^{-1}$, respectively) can be tentatively assigned to
507 the higher content of kaolinite in the V-IDP material.

508

509 ## 4. Concluding remarks and perspectives

510 The results obtained in this study confirm that illite du Puy is a suitable model clay system
511 almost solely constituted by illite clay mineral. Most of the variability in the characterization
512 data found in the literature originates from mineralogical variation that results from the different
513 locations of geological sampling. However, the particle size distribution between the different
514 subfractions is similar irrespective of the sampling location.

515 Precise sampling in the sedimentary Velay clay-rich formation allows for the extraction
516 of almost pure illite with a minor amount of non-clay phases. Using a suite of different
517 techniques, different size fractions of this illitic material used in the ongoing EURAD project

were fully characterized. This sample was found to be an illite–smectite mixed-layer material with an extremely low amount of smectite layers (<5%). No significant changes in crystal chemistry or particle aspect ratios were found between the different subfractions. These different subfractions displayed a wide range of specific surface areas (i.e., N_2 BET surface) and cation exchange capacity values, increasing by factors of ~3 and ~5 from the 0.2-2 µm to the <0.05 µm size fractions, respectively. EURAD illite and associated subfractions can thus be considered good models to better understand the adsorption and diffusion of solutes in clay-rich materials. The size fraction can be chosen to tune the specific surface area and thus enhance or reduce the anionic exclusion and adsorption effects of solutes in the case of diffusion studies of ionic tracers within compacted samples (Ochs et al., 2001; Sato and Suzuki, 2003; Van Loon et al., 2003, 2007; Appelo and Wersin, 2007; González Sánchez et al., 2008; Melkior et al., 2009; Glaus et al., 2010, 2011; Mazurek et al., 2011; Savoye et al., 2012, 2015; Altmann et al., 2015; Bestel et al., 2018). Such a variation is also important to experimentally highlight the role played by the electrical double layers located around particles in the diffusion of cations and anions. Finally, the similar aspect ratios and TSA values obtained for illite and vermiculite (Reinholdt et al., 2013) subfractions with comparable external CEC values represent key assets for the investigation of the influence of interlayer porosity on solute transport properties in porous media made of these two types of particles for a given particle size and morphology.

Acknowledgments

The results presented here are part of the PhD thesis of A.A. granted by "Région Nouvelle-Aquitaine", University of Poitiers, France. The "environmental mineralogy" platform at IC2MP is acknowledged. The authors are grateful to the European Joint Program EURAD (WP "Future" - grant ID 847593), the CNRS interdisciplinary "défi Needs" program (Project

DARIUS), the French government program “Investissements d’Avenir” (EUR INTREE, reference ANR-18-EURE-0010), and the European Union (ERDF) and “Région Nouvelle Aquitaine” for providing financial support for this study. Finally, this work was also partly carried out in the Pôle de compétences Physico-Chimie de l’Environnement, LIEC laboratory UMR 7360 CNRS – Université de Lorraine.

Supplementary Data (S.D.)

Table S1 reports the main parameters of Na^+-saturated EURAD illite du Puy (Na-EIDP) size fractions obtained by using the DIS method applied to low-pressure Ar adsorption isotherms.

Captions

Fig. 1. (a) Experimental X-ray diffraction patterns (black crosses) of randomly oriented Na^+-saturated bulk powders of Velay illite du Puy (V-IDP) and EURAD illite du Puy (E-IDP) together with calculated patterns obtained by BGMN Rietveld refinement (red solid lines). (b) Quantitative mineralogical composition (in wt. %) for the two types of samples as determined from Rietveld refinement with I: illite, K: kaolinite, K-Fd: potassium feldspar, Plag: plagioclase, Qz: quartz, Cal: calcite, Hal: halite, Ap: apatite, and Ana: anatase.

Fig. 2. Lithological section of the central zone of the Velay basin (adapted from Gabis, (1963)), illustrating the potential sampling locations of the two samples investigated in the present study. The experimental X-ray diffraction pattern from Gabis (1963) obtained for green clays alternating with gray marl banks, shown as an insert, is similar to that obtained in this study for the EURAD illite du Puy (E-IDP; top) considering the absence of kaolinite and calcite. The XRD pattern collected for Versicolor clays at the bottom of the middle series by Gabis (1963), also shown as an insert, with kaolinite and calcite as accessory minerals, is similar to the pattern obtained in this present study for Velay illite du Puy (V-IDP; bottom).

Fig. 3. Experimental X-ray diffraction patterns of oriented Ca^{2+}-saturated preparations for the different subfractions of Velay illite du Puy (V-IDP, left) and EURAD illite du Puy (E-IDP, right). In black, the patterns are recorded under air-dried conditions, whereas the patterns after ethylene glycol saturation are shown in gray. I and K stand for illite and kaolinite reflections, respectively. Non-indexed reflections are associated with accessory minerals.

588 **Fig. 4**. Comparison between the experimental (crosses) and calculated (solid red lines) XRD
589 patterns of oriented Ca^{2+}-saturated preparations recorded in air-dried (AD) and after ethylene
590 glycol (EG) saturation for the different subfractions of EURAD illite du Puy (E-IDP). The
591 structural parameters of the illite–smectite mixed-layer minerals are reported in Table 2.
592
593 **Fig. 5**. Experimental low-pressure Ar derivative adsorption isotherms (open circles) were
594 obtained at 77 K for the different Na^{+}-saturated subfractions of EURAD illite du Puy (E-IDP).
595 Derivative isotherm summation (DIS) decompositions are reported as dashed lines (red and
596 green for domains associated with Ar adsorption on basal and lateral surfaces, respectively).
597 The sum of the different DIS contributions is shown as a solid blue line.
598
599
600
601
602
603
604
605
606
607
608
609
610
611

5. References

Altmann, S., Aertsens, M., Appelo, T., Bruggeman, C., Gaboreau, S., Glaus, M., Jacquier, P., Kupcik, T., Maes, N., Montoya, V., Rabung, T., Savoye, S., et al, 2015. Processes of cation migration in clayrocks: Final Scientific Report of the CatClay European Project. CEA.

Appelo, C.A.J., Wersin, P., 2007. Multicomponent Diffusion Modeling in Clay Systems with Application to the Diffusion of Tritium, Iodide, and Sodium in Opalinus Clay. Environ. Sci. Technol. 41, 5002–5007. https://doi.org/10.1021/es0629256

Bakker, E., Lanson, B., Findling, N., Wander, M.M., Hubert, F., 2019. Mineralogical differences in a temperate cultivated soil arising from different agronomic processes and plant K-uptake. Geoderma 347, 210–219. https://doi.org/10.1016/j.geoderma.2019.04.010

Bardot, F., 1998. Les minéraux argileux et leur hétérogénéité superficielle : influence de la nature des cations compensateurs superficiels de l'illite sur les mécanismes d'adsorption de gaz. PhD, 241 pp. Institut National Polytechnique de Lorraine, Lorraine -France.

Bardot, F., Villiéras, F., Michot, L.J., Francois, M., Gérard, G., Cases, J.M., 1998. High resolution gas adsorption study on illites permuted with various cations : assessment of surface energetic properties. Journal of Dispersion Science and Technology 19, 739–759. https://doi.org/10.1080/01932699808913212

Bestel, M., Glaus, M.A., Frick, S., Gimmi, T., Juranyi, F., Van Loon, L.R., Diamond, L.W., 2018. Combined tracer through-diffusion of HTO and 22Na through Na-montmorillonite with different bulk dry densities. Applied Geochemistry 93, 158–166. https://doi.org/10.1016/j.apgeochem.2018.04.008

Bradbury, M.H., Baeyens, B., 2005. Experimental and Modelling Investigations on Na-Illite: Acid-Base Behaviour and the Sorption of Strontium, Nickel, Europium and Uranyl (Technical report No. 04–02). Paul Scherrer Institut, Villigen.

Bradbury, M.H., Baeyens, B., 2009. Sorption modelling on illite Part I: Titration measurements and the sorption of Ni, Co, Eu and Sn. Geochimica et Cosmochimica Acta 73, 990–1003. https://doi.org/10.1016/j.gca.2008.11.017

Chagneau, A., Tournassat, C., Steefel, C.I., Bourg, I.C., Gaboreau, S., Esteve, I., Kupcik, T., Claret, F., Schäfer, T., 2015. Complete Restriction of $^{36}Cl^-$ Diffusion by Celestite Precipitation in Densely Compacted Illite. Environ. Sci. Technol. Lett. 2, 139–143. https://doi.org/10.1021/acs.estlett.5b00080

Chemeda, Y.C., Deneele, D., Razafitianamaharavo, A., Villiéras, F., Ouvrard, G., 2021. Assessment of surface heterogeneity of lime treated kaolinites: Probed by low-pressure argon and nitrogen gas adsorption. Applied Clay Science 206, 106069. https://doi.org/10.1016/j.clay.2021.106069

Diaz, N., 2009. Modélisation prédictive de la migration des anions par description de la microstructure de la roche : application à l'argilite du Callovo-Oxfordien. Université Paris 6, France.

Doebelin, N., Kleeberg, R., 2015. Profex: a graphical user interface for the Rietveld refinement program BGMN. J. Appl. Crystallogr. 48, 1573–1580. https://doi.org/10.1107/S1600576715014685

Drits, V., 1997. XRD Measurement of Mean Crystallite Thickness of Illite and Illite/Smectite: Reappraisal of the Kubler Index and the Scherrer Equation. Clays and Clay Minerals 45, 461–475. https://doi.org/10.1346/CCMN.1997.0450315

Ferrage, E., Vidal, O., Mosser-Ruck, R., Cathelineau, M., Cuadros, J., 2011. A reinvestigation of smectite illitization in experimental hydrothermal conditions: Results from X-ray diffraction and transmission electron microscopy. American Mineralogist 96, 207–223. https://doi.org/10.2138/am.2011.3587

Gabis, V., 1963. Étude minéralogique et géochimique de la série sédimentaire oligocène du Velay. Bulletin de la Société française de Minéralogie et de Cristallographie 86, 315–354. https://doi.org/10.3406/bulmi.1963.5663

Glaus, M.A., Aertsens, M., Maes, N., Van Laer, L., Van Loon, L.R., 2015. Treatment of boundary conditions in through-diffusion: A case study of 85Sr2+ diffusion in compacted illite. Journal of Contaminant Hydrology 177–178, 239–248. https://doi.org/10.1016/j.jconhyd.2015.03.010

Glaus, M.A., Frick, S., Rossé, R., Loon, L.R.V., 2010. Comparative study of tracer diffusion of HTO, $^{22}Na^{+}$ and $^{36}Cl^{-}$ in compacted kaolinite, illite and montmorillonite. Geochimica et Cosmochimica Acta 74, 1999–2010. https://doi.org/10.1016/j.gca.2010.01.010

Glaus, M.A., Frick, S., Rossé, R., Van Loon, L.R., 2011. Consistent interpretation of the results of through-, out-diffusion and tracer profile analysis for trace anion diffusion in compacted montmorillonite. Journal of Contaminant Hydrology 123, 1–10. https://doi.org/10.1016/j.jconhyd.2010.11.009

González Sánchez, F., Van Loon, L.R., Gimmi, T., Jakob, A., Glaus, M.A., Diamond, L.W., 2008. Self-diffusion of water and its dependence on temperature and ionic strength in highly compacted montmorillonite, illite and kaolinite. Applied Geochemistry 23, 3840–3851. https://doi.org/10.1016/j.apgeochem.2008.08.008

Hassan, M.S., Villieras, F., Gaboriaud, F., Razafitianamaharavo, A., 2005. AFM and low-pressure argon adsorption analysis of geometrical properties of phyllosilicates. Journal of Colloid and Interface Science 296, 614–623. https://doi.org/10.1016/j.jcis.2005.09.028

Howard, S.A., Preston, K.D., 1989. Profile Fitting of Powder Diffraction Patterns, in: Modern Powder Diffraction; Bish, D. L., Post, J. E., Eds., Reviews in Mineralogy. Mineralogical Society of America, Washington, DC, pp. 217–275.

Hubert, F., Caner, L., Meunier, A., Ferrage, E., 2012. Unraveling complex <2 m clay mineralogy from soils using X-ray diffraction profile modeling on particle-size sub-fractions: Implications for soil pedogenesis and reactivity. American Mineralogist 97, 384–398. https://doi.org/10.2138/am.2012.3900

Kleeberg, R., Monecke, T., Hillier, S., 2008. Preferred Orientation of Mineral Grains in Sample Mounts for Quantitative XRD Measurements: How Random are Powder Samples? Clays Clay Miner. 56, 404–415. https://doi.org/10.1346/CCMN.2008.0560402

Mazurek, M., Alt-Epping, P., Bath, A., Gimmi, T., Niklaus Waber, H., Buschaert, S., Cannière, P.D., Craen, M.D., Gautschi, A., Savoye, S., Vinsot, A., Wemaere, I., Wouters, L., 2011. Natural tracer profiles across argillaceous formations. Applied Geochemistry 26, 1035–1064. https://doi.org/10.1016/j.apgeochem.2011.03.124

Melkior, T., Gaucher, E.C., Brouard, C., Yahiaoui, S., Thoby, D., Clinard, Ch., Ferrage, E., Guyonnet, D., Tournassat, C., Coelho, D., 2009. Na^{+} and HTO diffusion in compacted bentonite: Effect of surface chemistry and related texture. Journal of Hydrology 370, 9–20. https://doi.org/10.1016/j.jhydrol.2009.02.035

Michot, L., Francois, M., Cases, J.M., 1990. Surface heterogeneity studied by a quasi-equilibrium gas adsorption procedure. Langmuir 6, 677–681. https://doi.org/10.1021/la00093a025

Moore, D.M., Reynolds, R.C.J., 1997. X-ray Diffraction and the Identification and Analysis of Clay Minerals. Oxford University Press.

Ochs, M., Lothenbach, B., Wanner, H., Sato, H., Yui, M., 2001. An integrated sorption–diffusion model for the calculation of consistent distribution and diffusion coefficients in compacted bentonite. Journal of Contaminant Hydrology 47, 283–296. https://doi.org/10.1016/S0169-7722(00)00157-1

Poinssot, C., Baeyens, B., Bradbury, M.H., 1999. Experimental and modelling studies of caesium sorption on illite. Geochimica et Cosmochimica Acta 63, 3217–3227. https://doi.org/10.1016/S0016-7037(99)00246-X

Rabung, Th., Pierret, M.C., Bauer, A., Geckeis, H., Bradbury, M.H., Baeyens, B., 2005. Sorption of Eu(III)/Cm(III) on Ca-montmorillonite and Na-illite. Part 1: Batch sorption and time-resolved laser fluorescence spectroscopy experiments. Geochimica et Cosmochimica Acta 69, 5393–5402. https://doi.org/10.1016/j.gca.2005.06.030

Rajec, P., Sucha, V., Eberl, D.D., Srodon, J., Elsass, F., 1999. Effect of Illite Particle Shape on Cesium Sorption. Clays and Clay Minerals 47, 755–760. https://doi.org/10.1346/CCMN.1999.0470610

Rajyaguru, A., 2018. Impact of saline plume on containment properties of natural porous materials in geological disposal context: An experimental and REV simulation approach to go beyond Archie's law. PhD, 295 pp. PSL Research University, Paris, France.

Reinholdt, M.X., Hubert, F., Faurel, M., Tertre, E., Razafitianamaharavo, A., Francius, G., Prêt, D., Petit, S., Béré, E., Pelletier, M., Ferrage, E., 2013. Morphological properties of vermiculite particles in size-selected fractions obtained by sonication. Applied Clay Science 77–78, 18–32. https://doi.org/10.1016/j.clay.2013.03.013

Robert, M., Hardy, M., Elsass, F., 1991. Crystallochemistry, properties and organization of soil clays derived from major sedimentary rocks in France. Clay miner. 26, 409–420. https://doi.org/10.1180/claymin.1991.026.3.09

Sakharov, A., Naumov, A.S., Drits, V.A., 1982a. X-ray diffraction by mixed-layer structures with random distribution of stacking faults. Dokl. Akad. Nauk 265, 339–343.

Sakharov, A., Naumov, A.S., Drits, V.A., 1982b. X-ray intensities scattered by layer structures with short-range ordering parameters $S \geq 1$ and $G \geq 1$. Dokl. Akad. Nauk 265, 871–874.

Sakharov, A., Naumov, A.S., Drits, V.A., 1983. X-ray scattering by defect layer structures. Kristallografia 28, 951–958.

Sato, H., Suzuki, S., 2003. Fundamental study on the effect of an orientation of clay particles on diffusion pathway in compacted bentonite. Applied Clay Science 23, 51–60. https://doi.org/10.1016/S0169-1317(03)00086-3

Savoye, S., Beaucaire, C., Grenut, B., Fayette, A., 2015. Impact of the solution ionic strength on strontium diffusion through the Callovo-Oxfordian clayrocks: An experimental and modeling study. Applied Geochemistry 61, 41–52. https://doi.org/10.1016/j.apgeochem.2015.05.011

Savoye, S., Frasca, B., Grenut, B., Fayette, A., 2012. How mobile is iodide in the Callovo–Oxfordian claystones under experimental conditions close to the in situ ones? Journal of Contaminant Hydrology 142–143, 82–92. https://doi.org/10.1016/j.jconhyd.2012.10.003

Tertre, E., Ferrage, E., Bihannic, I., Michot, L.J., Prêt, D., 2011a. Influence of the ionic strength and solid/solution ratio on Ca(II)-for-Na+ exchange on montmorillonite. Part 2: Understanding the effect of the m/V ratio. Implications for pore water composition and element transport in natural media. Journal of Colloid and Interface Science 363, 334–347. https://doi.org/10.1016/j.jcis.2011.07.003

Tertre, E., Prêt, D., Ferrage, E., 2011b. Influence of the ionic strength and solid/solution ratio on Ca(II)-for-Na^+ exchange on montmorillonite. Part 1: Chemical measurements, thermodynamic modeling and potential implications for trace elements geochemistry. Journal of Colloid and Interface Science 353, 248–256. https://doi.org/10.1016/j.jcis.2010.09.039

Tessier, M., 1984. Etude expérimentale de l'organisation des matériaux argileux: Hydratation, gonflement et structuration au cours de la dessiccation et de la réhumectation. INRA.

Van Loon, L.R., Glaus, M.A., Müller, W., 2007. Anion exclusion effects in compacted bentonites: Towards a better understanding of anion diffusion. Applied Geochemistry 22, 2536–2552. https://doi.org/10.1016/j.apgeochem.2007.07.008

Van Loon, L.R., Soler, J.M., Jakob, A., Bradbury, M.H., 2003. Effect of confining pressure on the diffusion of HTO, $36Cl^-$ and $125I^-$ in a layered argillaceous rock (Opalinus Clay): diffusion perpendicular to the fabric. Applied Geochemistry 18, 1653–1662. https://doi.org/10.1016/S0883-2927(03)00047-7

Viennet, J.-C., Hubert, F., Ferrage, E., Tertre, E., Legout, A., Turpault, M.-P., 2015. Investigation of clay mineralogy in a temperate acidic soil of a forest using X-ray diffraction profile modeling: Beyond the HIS and HIV description. Geoderma 241–242, 75–86. https://doi.org/10.1016/j.geoderma.2014.11.004

Viennet, 2015. Minéraux argileux aluminisés des sols : caractérisation structurale par modélisation des diffractogrammes de rayons X et détermination des mécanismes de formation par approche expérimentale. PhD, 190 pp. Université de Poitiers, France.

Villieras, F., Cases, J.M., Francois, M., Michot, L.J., Thomas, F., 1992. Texture and surface energetic heterogeneity of solids from modeling of low pressure gas adsorption isotherms. Langmuir 8, 1789–1795. https://doi.org/10.1021/la00043a018

Villieras, F., Michot, L.J., Bardot, F., Cases, J.M., François, M., Rudziński, W., 1997. An Improved Derivative Isotherm Summation Method To Study Surface Heterogeneity of Clay Minerals. Langmuir 13, 1104–1117. https://doi.org/10.1021/la9510083

Wilson, M.J., 2013. Rock-forming Minerals, Sheet Silicates: Clay Minerals, Second. ed. Geological Society of London, London.

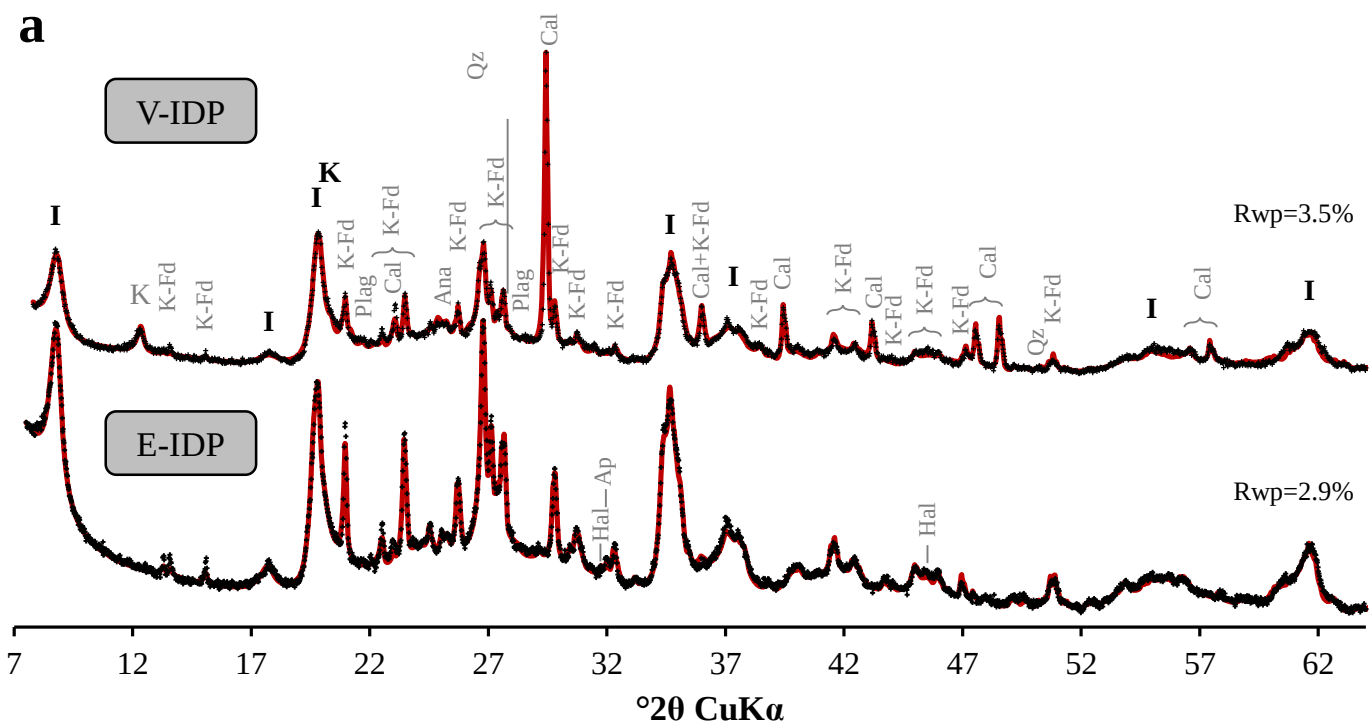
a
V-IDP
E-IDP
Rwp=3.5%
Rwp=2.9%
Qz
Cal
K-Fd
Plag
Ana
Cal+K-Fd
Hal—Ap
Hal
7
12
17
22
27
32
37
42
47
52
57
62
°2θ CuKα

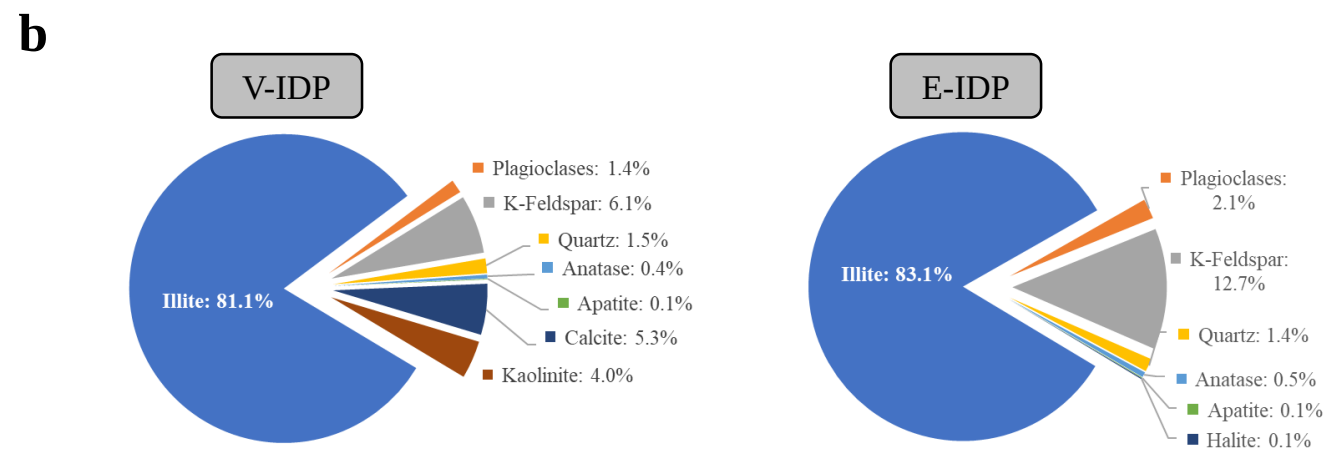
b
V-IDP
Illite: 81.1%
Plagioclases: 1.4%
K-Feldspar: 6.1%
Quartz: 1.5%
Anatase: 0.4%
Apatite: 0.1%
Calcite: 5.3%
Kaolinite: 4.0%
E-IDP
Illite: 83.1%
Plagioclases: 2.1%
K-Feldspar: 12.7%
Quartz: 1.4%
Anatase: 0.5%
Apatite: 0.1%
Halite: 0.1%

Fig. 1.

Central zone of Velay basin

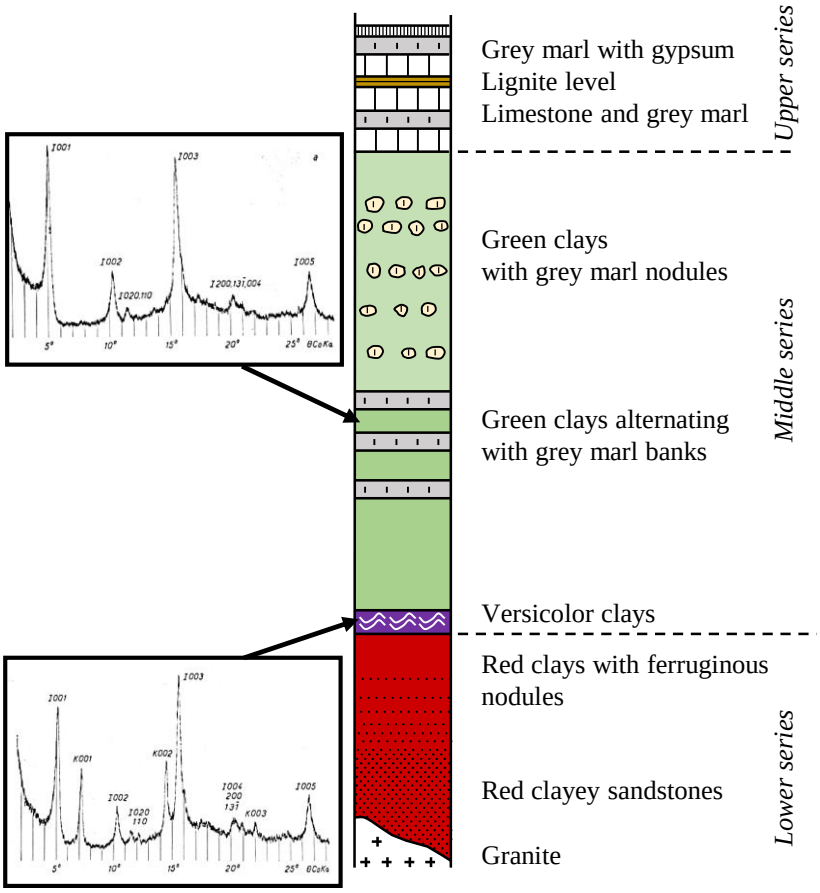

Fig. 2.

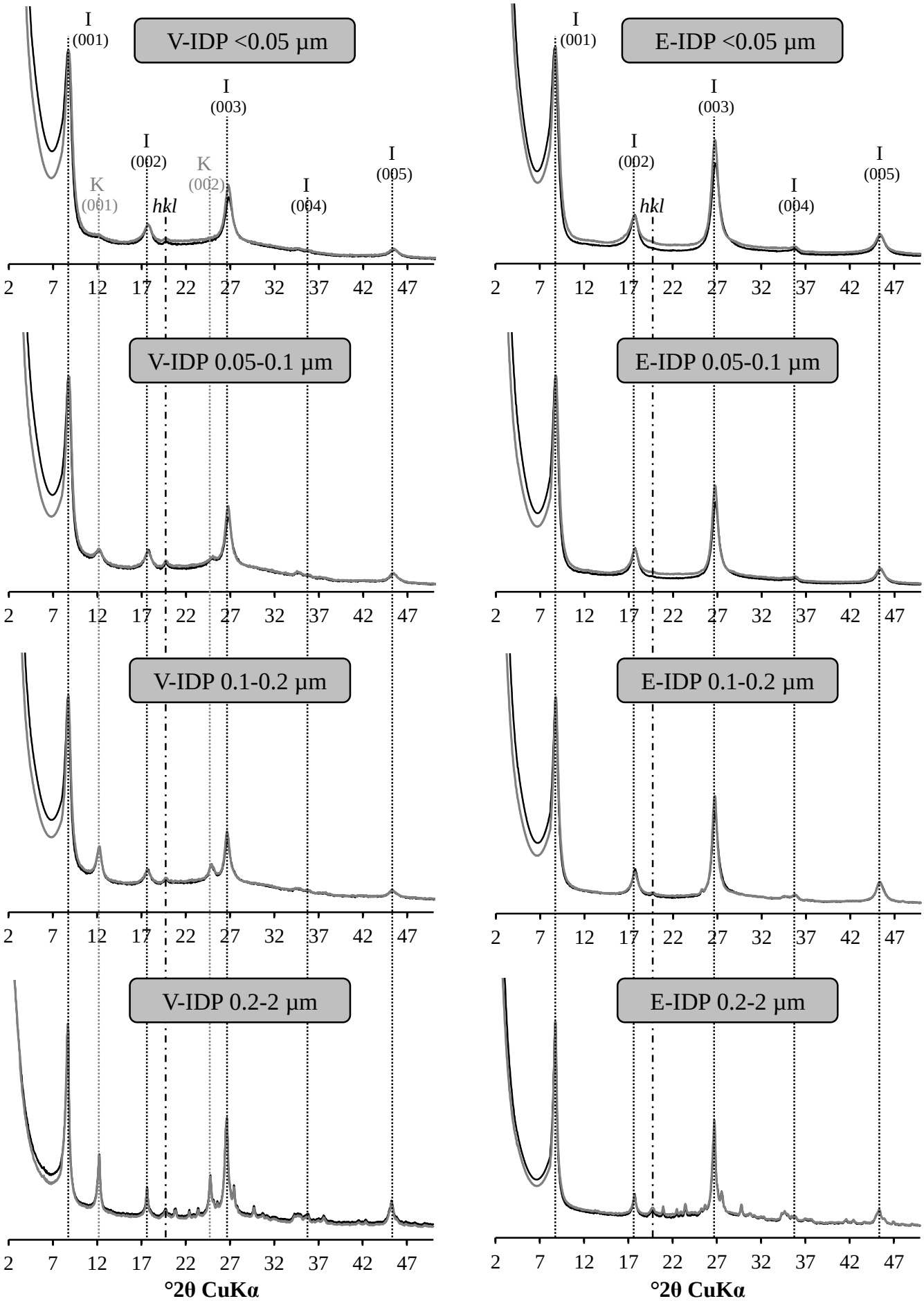
V-IDP <0.05 µm
E-IDP <0.05 µm
V-IDP 0.05-0.1 µm
E-IDP 0.05-0.1 µm
V-IDP 0.1-0.2 µm
E-IDP 0.1-0.2 µm
V-IDP 0.2-2 µm
E-IDP 0.2-2 µm
I (001)
I (002)
I (003)
I (004)
I (005)
K (001)
K (002)
hkl
2 7 12 17 22 27 32 37 42 47
°2θ CuKα

Fig. 3.

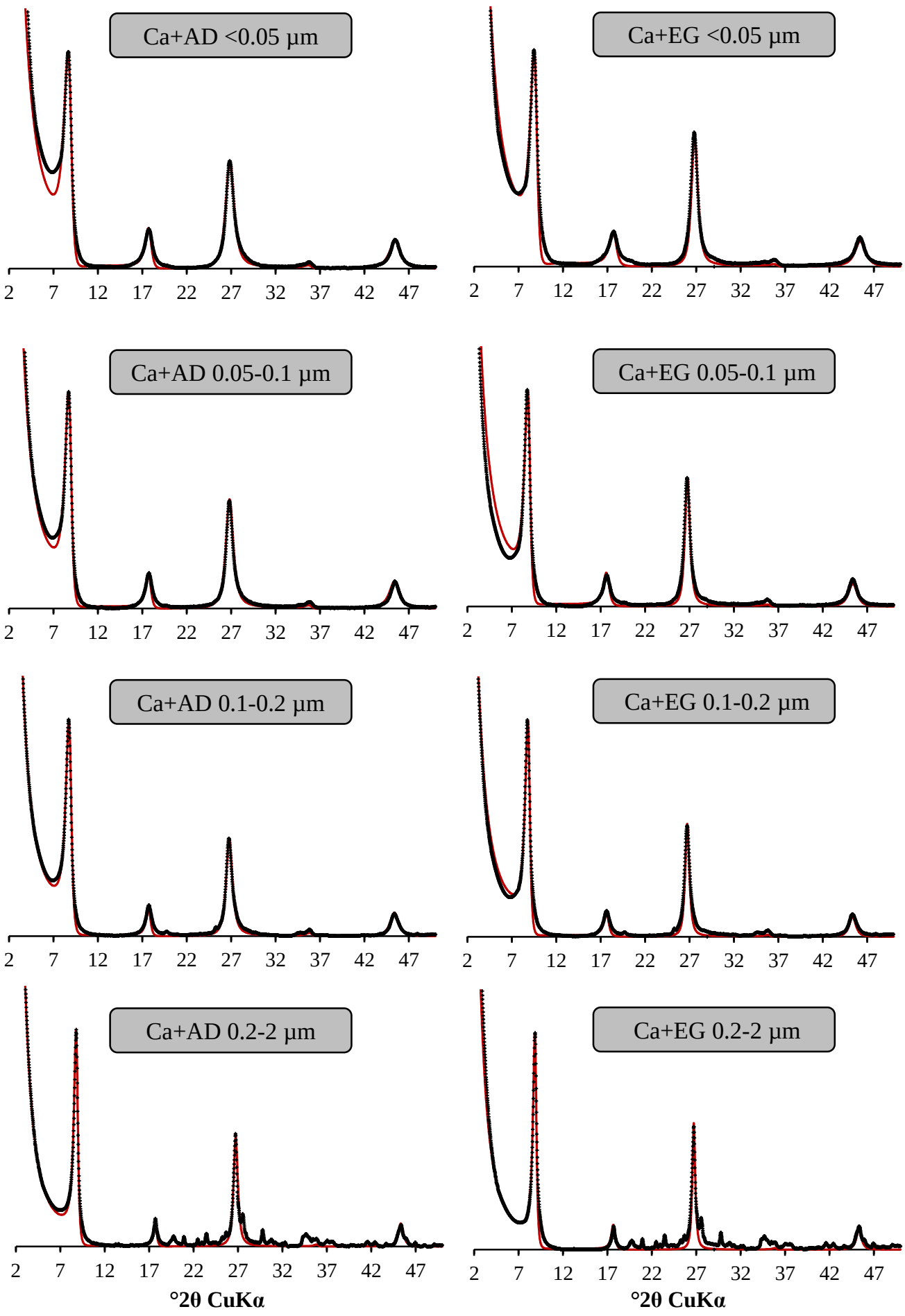
Ca+AD <0.05 µm
Ca+EG <0.05 µm
Ca+AD 0.05-0.1 µm
Ca+EG 0.05-0.1 µm
Ca+AD 0.1-0.2 µm
Ca+EG 0.1-0.2 µm
Ca+AD 0.2-2 µm
Ca+EG 0.2-2 µm
2 7 12 17 22 27 32 37 42 47
°2θ CuKα

Fig. 4.

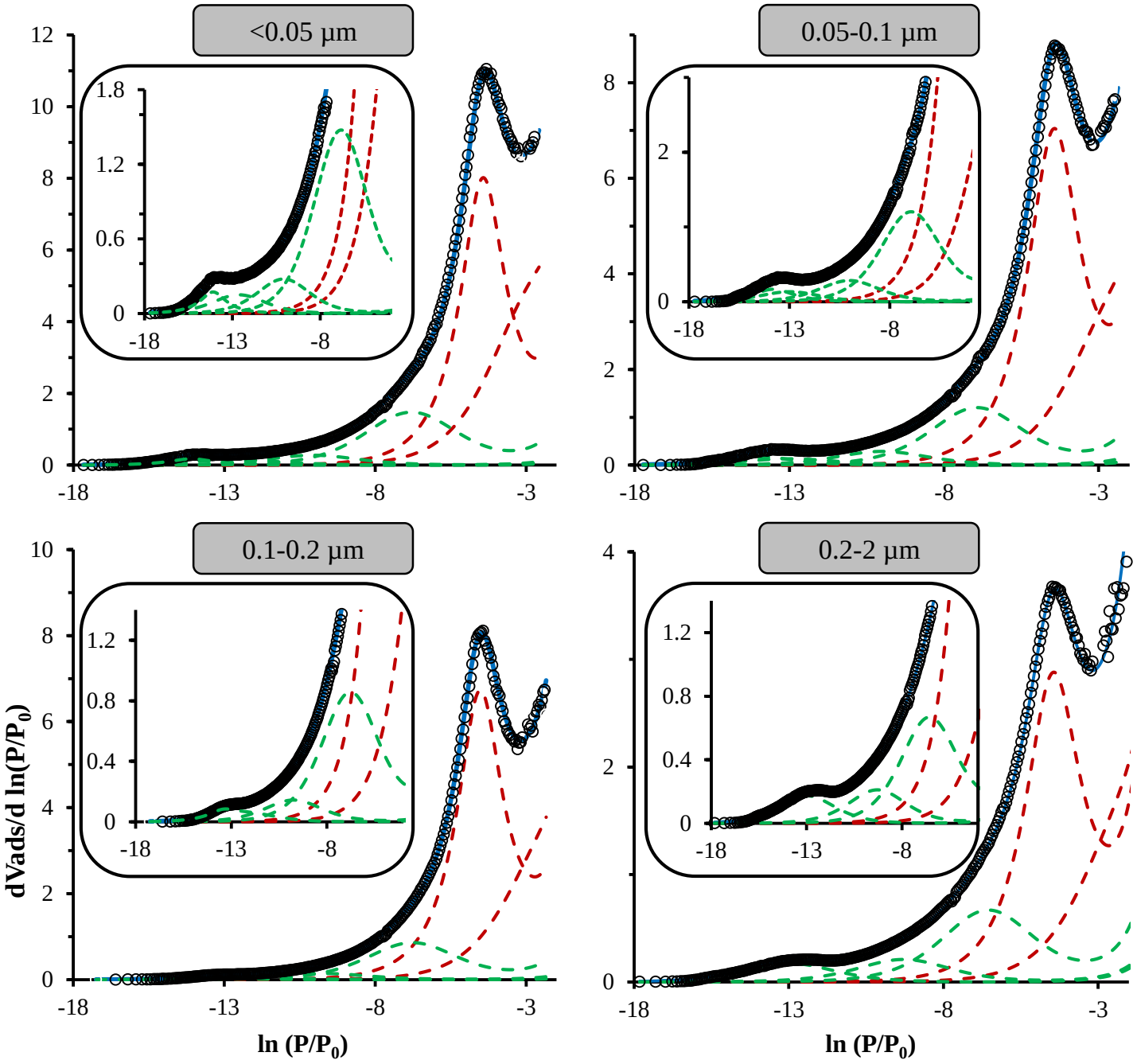

Fig. 5.